The Astrophysical Journal, 851:81 (8pp), 2017 December 20 https://doi.org/10.3847/1538-4357/aa9845

Mass Profile Decomposition of the Frontier Fields Cluster MACS J0416-2403: Insights on the Dark-matter Inner Profile

M. Annunziatella[1], M. Bonamigo[2], C. Grillo[3,2], A. Mercurio[4], P. Rosati[5], G. Caminha[5,6], A. Biviano[1], M. Girardi[7], R. Gobat[8], M. Lombardi[5], and E. Munari[1]
[1] INAF-Osservatorio Astronomico di Trieste, via G. B. Tiepolo 11, Trieste, Italy; marianna.annunziatella@gmail.com
[2] Dark Cosmology Centre, Niels Bohr Institute, University of Copenhagen, Juliane Maries Vej 30, DK-2100 Copenhagen, Denmark
[3] Dipartimento di Fisica, Università degli Studi di Milano, via Celoria 16, I-20133 Milan, Italy
[4] INAF-Osservatorio Astronomico di Capodimonte, Via Moiariello 16 I-80131 Napoli, Italy
[5] Dipartimento di Fisica e Scienze della Terra, Univ. degli Studi di Ferrara, via Saragat 1, I-44122, Ferrara, Italy
[6] INAF—Osservatorio Astronomico di Bologna, via Gobetti 93/3, I-40129 Bologna, Italy
[7] Dipartimento di Fisica, Univ. degli Studi di Trieste, via Tiepolo 11, I-34143 Trieste, Italy
[8] Korea Institute for Advanced Study, KIAS, 85 Hoegiro, Dongdaemun-gu Seoul 130-722, Korea
Received 2017 August 30; revised 2017 October 17; accepted 2017 October 19; published 2017 December 14

Abstract

We present a high-resolution dissection of the two-dimensional total mass distribution in the core of the Hubble Frontier Fields galaxy cluster MACS J0416.1−2403, at $z = 0.396$. We exploit *HST*/WFC3 near-IR (F160W) imaging, VLT/Multi Unit Spectroscopic Explorer spectroscopy, and *Chandra* data to separate the stellar, hot gas, and dark-matter mass components in the inner 300 kpc of the cluster. We combine the recent results of our refined strong lensing analysis, which includes the contribution of the intracluster gas, with the modeling of the surface brightness and stellar mass distributions of 193 cluster members, of which 144 are spectroscopically confirmed. We find that, moving from 10 to 300 kpc from the cluster center, the stellar to total mass fraction decreases from 12% to 1% and the hot gas to total mass fraction increases from 3% to 9%, resulting in a baryon fraction of approximatively 10% at the outermost radius. We measure that the stellar component represents ∼30%, near the cluster center, and 15%, at larger clustercentric distances, of the total mass in the cluster substructures. We subtract the baryonic mass component from the total mass distribution and conclude that within 30 kpc (∼3 times the effective radius of the brightest cluster galaxy) from the cluster center the surface mass density profile of the total mass and global (cluster plus substructures) dark-matter are steeper and that of the diffuse (cluster) dark-matter is shallower than an NFW profile. Our current analysis does not point to a significant offset between the cluster stellar and dark-matter components. This detailed and robust reconstruction of the inner dark-matter distribution in a larger sample of galaxy clusters will set a new benchmark for different structure formation scenarios.

Key words: dark matter – galaxies: clusters: general – galaxies: clusters: individual (MACS J0416.1-2403)

1. Introduction

One of the main achievements of the current ΛCDM cosmological paradigm is to be able to describe the large-scale distribution of matter in the universe at different epochs (Springel et al. 2006). Cosmological *N*-body simulations implemented within the ΛCDM paradigm have provided precise predictions on the formation and evolution of dark-matter halos over a wide range of scales. A key result of these simulations is that dark-matter halos of all masses have "universal" mass density profiles that are well described by a simple law with a central cusp $\rho(r) \sim r^{-1}$, and a steeper slope, $\rho(r) \sim r^{-3}$, at large radii (the so-called NFW profile; Navarro et al. 1996). Despite the great success of the ΛCDM predictions, some discrepancies with available observations still exist.

Some tension between the observed and predicted values of the inner slope of the dark-matter mass density profile has been detected at two extremes of the halo mass distribution: dwarf galaxies and galaxy clusters. In the past few years, significant progress has been made toward the measurement of the value of the inner logarithmic slope ($\gamma_{\rm in}$) of the dark-matter mass profile in clusters, but, in some cases, the results obtained by different groups on the same clusters are still controversial. For example, Okabe & Smith (2016) find that 50 X-ray luminous galaxy clusters with good gravitational lensing data have a stacked total mass density profile consistent with the NFW profile from the inner core to the virial radius. Similarly, Umetsu et al. (2016) conclude that the stacked total mass density profile of 16 massive clusters in the Cluster Lensing And Supernova survey with Hubbe (CLASH; Postman et al. 2012) survey is well described by an NFW profile. On the other hand, Newman et al. (2013a, 2013b) find that the total mass density profile in the center of clusters closely follows the NFW profile but, once the contribution of the stellar component is subtracted, the inferred dark-matter mass density profile is significantly flatter than an NFW profile. On smaller scales, dwarf galaxies are studied in the same context because their very high mass-to-light ratios (M/Ls) suggest that baryonic effects may have been minor in their mass assembly history. Dynamical analyses of dwarf and low surface brightness galaxies seem to favor massive dark-matter halos with surprisingly shallow or cored ($\gamma_{\rm in} \ll 1$) inner density profiles (e.g., Agnello & Evans 2012; Amorisco & Evans 2012), whereas much steeper ($\gamma_{\rm in} \sim 2$) profiles are preferred in massive early-type galaxies from strong gravitational lensing and stellar population modeling (e.g., Grillo 2012).

These debated results are also known as the dark-matter cusp-core problem. The value of $\gamma_{\rm in}$ could contain important information about the nature of the dark matter. For example, if the dark-matter particles were self-interacting rather than effectively collisionless, with a sufficiently large self-interaction

cross-section, the inner halo mass density profile should be shallower than an NFW profile (Navarro et al. 1996), in the absence of baryonic effects (Rocha et al. 2013). A major leap forward in addressing these fundamental questions can only be made by obtaining homogeneous, high quality data on a sizable and unbiased sample of astrophysical objects. Clusters of galaxies, by virtue of their position at the high end of the mass function, serve as giant physics laboratories to explore the role and nature of dark matter, providing unique tests of any viable cosmology and structure formation scenario and possible modifications of the laws of gravity. Furthermore, massive clusters offer this unique opportunity, as a number of observational probes of their mass profiles can be used to robustly check the ΛCDM predictions on a large dynamical range of densities and distances from the cluster centers.

The main goal of this paper is to disentangle the dark-matter distribution in the massive galaxy cluster MACS J0416.1 −2403 (hereafter M0416) and to measure the values of the inner slope of the cluster dark-matter halo. In this study, we present for the first time an accurate determination of the stellar, hot gas, and total projected mass density profiles out to 300 kpc from the cluster center. Hence we are able to separate the baryonic and dark-matter components from the cluster total mass distribution. We are also able to evaluate the fractions of the different components relative to the total mass of the cluster.

This paper is organized as follows. In Section 2, we briefly introduce the photometric and spectroscopic data used in this work. In Section 3, we describe how we derive the stellar mass profile of M0416. In Section 4, we analyze the distribution of different cluster components. In Section 5, we focus on the dark-matter component of M0416. Finally, in Section 6, we draw our conclusions.

Throughout this paper, we use $H_0 = 70\,\mathrm{km\,s^{-1}\,Mpc^{-1}}$, $\Omega_M = 0.3$, and $\Omega_\Lambda = 0.7$. At the cluster redshift, the scale is $321\,\mathrm{kpc\,arcmin^{-1}}$. All the magnitudes used in this work are referred to the AB system.

2. Data Sample

M0416 is a massive galaxy cluster first detected by Ebeling et al. (2001). This cluster has been imaged with *HST* for a total of 25 orbits using 16 different filters as a part of the CLASH survey. M0416 has also been observed with the VIsible Multi-Object Spectrograph (VIMOS) at the ESO/VLT, as part of the ESO Large Programme "Dark Matter Mass Distributions of Hubble Treasury Clusters and the Foundations of ΛCDM Structure Formation Models" (CLASH-VLT; Rosati et al. 2014). CLASH-VLT collected a large sample of spectra for galaxies in the field of view of this cluster, leading to the spectroscopic confirmation of ∼800 cluster members and to the discovery of multiply imaged background sources. More details on VIMOS spectroscopic data can be found in Balestra et al. (2016). These data have been used to obtain a precise total reconstruction of the cluster via gravitational strong lensing modeling (Grillo et al. 2015).

M0416 was then selected to be reobserved, as part of the Hubble Frontier Fields (HFF) initiative (Lotz et al. 2016), in ACS/optical (F435W, F606W, and F814W) and WFC3/IR (F105W, F125W, F140W, and F160W) filters, for a total of 140 orbits, reaching a detection limit of ∼29 mag (AB) at 5σ for point sources. These observations of M0416 were completed in September 2014 (see, e.g., Jauzac et al. 2014). In all filters, mosaics are available with 30 and 60 mas pixel scale.

M0416 was later observed with the Multi Unit Spectroscopic Explorer (MUSE) at the VLT. In this work, we exploit MUSE archival data obtained from two different programs, which covered the northeast (NE) and southwest (SW) regions of the cluster. A detailed description of the MUSE data reduction and analysis is given in Caminha et al. (2017).

Here, we use the sample of cluster members also considered in Bonamigo et al. (2017, hereafter Bo17), including 193 galaxies, 144 with spectroscopic redshifts, and the others selected based on their *N*-dimensional distance, in color space, from the locus of the spectroscopically confirmed member galaxies (see Grillo et al. 2015 for more details).

2.1. Stellar Masses

In Grillo et al. (2015), the *HST* photometry available from the CLASH survey was used to determine the stellar mass values of a subsample of our catalog of spectroscopic members. In that paper, the images of the cluster in the reddest *HST* bands (from F435W to F160W) were used to perform a fit of the spectral energy distributions (SEDs) of these galaxies. The SED fitting was performed using composite stellar population models, based on Bruzual & Charlot (2003) templates, with solar metallicity and a Salpeter (1955) stellar initial mass function (IMF). The star formation histories used were parametrized as delayed exponential functions and the presence of dust was taken into account following Calzetti et al. (2000). For each galaxy, the best-fit ($M_\star^{\rm best}$) and 1σ lower ($M_\star^{\rm low}$) and upper limit ($M_\star^{\rm high}$) values of the stellar mass were measured. An example of an SED is shown in Figure 6 of Grillo et al. (2015). In Annunziatella et al. (2014, 2016), we have shown that we reached an accuracy of 10% in stellar masses down to $10^9\,M_\odot$, thanks to the multi-band *HST* photometry.

3. Mass Profiles

In this section, we describe how we derive the two-dimensional stellar mass distribution of the cluster members. We use the following approach: we reconstruct the surface brightness distribution of all member galaxies in the reddest *HST* band (F_{160}), then we use the best-fit values of the stellar masses of the subsample of galaxies discussed in Section 2.1 to derive an average stellar $M_\star/L$ for all cluster members. Cluster members have a $M_\star/L \sim 0.5$ in the F_{160} band, without significant variations over the probed stellar mass range. This $M_\star/L$ is hence used to convert the cluster cumulative luminosity profile into a cumulative stellar mass profile.

3.1. Surface Brightness Profiles

To determine the surface brightness profile of each cluster member, we use an iterative approach based on the two software: *galfit* (Peng et al. 2010) and `GALAPAGOS` (Barden et al. 2012). *Galfit* is a code to model the surfaces brightness profile of galaxies, while `GALAPAGOS` is a set of procedures that use *galfit* to reconstruct the surface brightness profile of all extended sources detected by SExtractor in a image (Bertin & Arnouts 1996). In this automatic run of *galfit*, we adopt a Sérsic profile for each galaxy. In the following, we briefly describe our method.

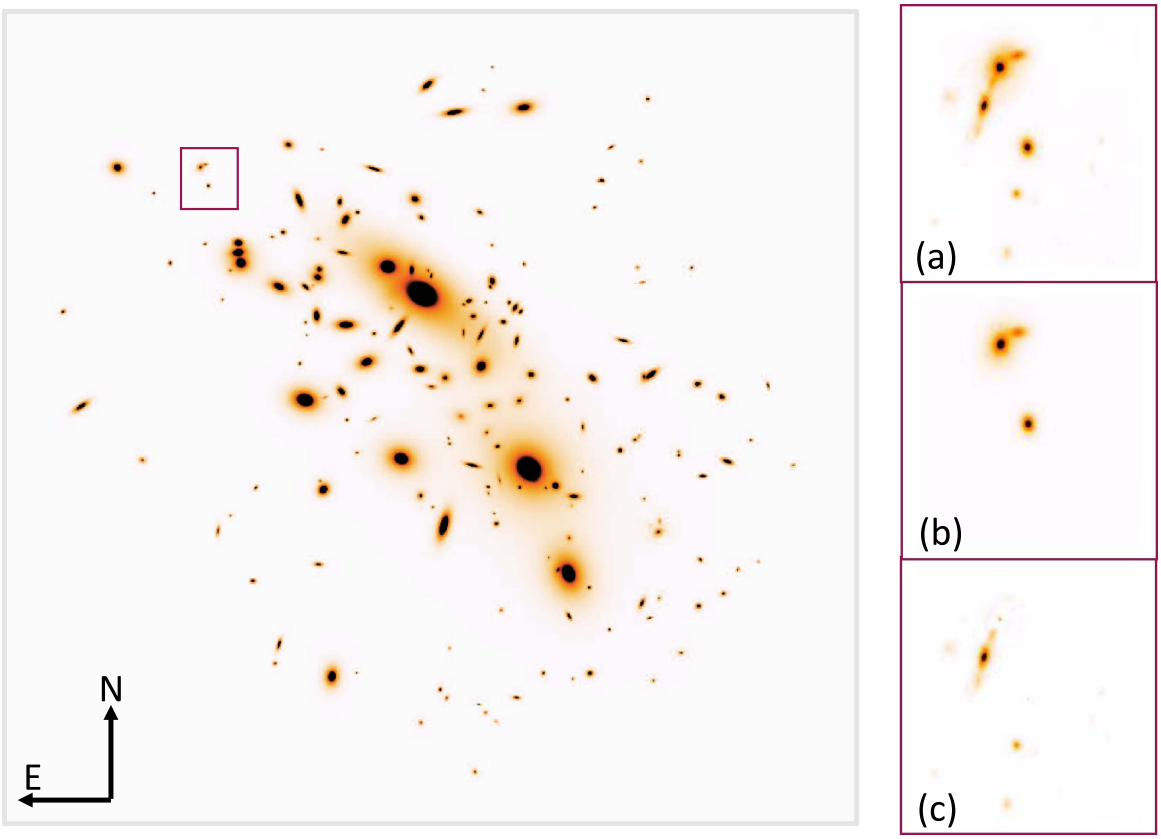

Figure 1. Left: model image of all cluster members before the convolution with the PSF. The image is 2 × 2 arcmin and covers the entire *HST* field of view. Right: original, model, and residual images of some interacting sources (top, middle, and bottom panel respectively) corresponding to the selection box in the main image (∼9 × 9 arcsec). The seven sources in the original and residual images are foreground/background galaxies, which have not been modeled.

1. We run GALAPAGOS on the *HST* image of the cluster, in the F_{160} band, with a pixel size of 60 mas pixel^{-1}. We choose not to use the image with the highest angular resolution since we are more interested in the global surface brightness model of the cluster than in the detailed structure of single galaxies. The input PSF is derived from real stars in the *HST* field from images with the 30 mas pixel scale. Therefore, we set the input parameter PSF_OVERSAMPLING to 2.
2. We then use the parameters coming from the first run of GALAPAGOS as input parameters to perform a Sérsic fit of just cluster members and very close galaxies, which could affect the photometry of the members. To do this, we divide our image into large stamps containing approximately 10 galaxies each and use *galfit* on these subimages. We use segmentation maps as *bad pixel masks* to identify the objects to fit in each stamp. We also fix the value of the sky background to 2×10^{-3}, which is the mean value that we obtain in empty small regions of the image.
3. Once the values of the model parameters of all galaxies in each stamp are stable, we perform a global fit of all the sources identified in the previous step. The result of this global fit shows a diffuse component, mainly between the two brightest cluster galaxies (BCGs) of the cluster, that can be associated to the intracluster light (ICL). For this reason, we add an extra source modeled in input with a Sérsic profile with $n = 1$. In this step, we fix all sources except those of the ICL and the two BCGs.
4. Finally, we run *galfit* again on the global image using the parameters of the ICL and the BCGs determined in the previous step.

With this procedure, we derive for all cluster members the best-fit values of the parameters of a Sérsic model (i.e., the effective radius, the magnitude within that radius, the Sérsic index, the minor to major axis ratio, and its position angle).

We perform several tests to confirm that our fits are robust. In particular, we check that using different PSFs the best-fit values of the parameters obtained for each galaxy are consistent within the errors and that the global residual image remains unaltered. In the left panel of Figure 1, we show the model image of all selected cluster members plus the ICL in M0416. An example of the goodness of our fits is shown on the right of Figure 1. Panel (a) shows a stamp of the original image containing three cluster members and seven foreground/background galaxies. Panel (b) shows the model image of just the member galaxies, and Panel (c) shows the residual (i.e., observed minus model) image.

3.2. Stellar Mass-to-light Ratio

We use the sample of spectroscopically confirmed members for which we have measured the stellar mass values (see Section 2.1) to calibrate the average $M_\star/L$ of all cluster members. From the 62 cluster members with stellar mass estimates, we exclude three objects that are outside the HFF field of view and two objects that show uncommonly high residuals in the fit. The faintest object in this sample has a magnitude of ∼23 mag in the F_{160} band. We sum the best-fit

stellar mass values of the 57 members and divide this quantity by the total luminosity of the same galaxies estimated from our surface brightness modeling. We also employ the values of $M_*^{\rm low}$ and $M_*^{\rm high}$ to derive a minimum and a maximum average stellar $M_\star/L$. To estimate the stellar mass values of all cluster members and thus the stellar mass map of the cluster, we use the global model image produced by *galfit* before the convolution with the PSF and with a zero background and multiply for with the average stellar $M_\star/L$s determined previously.

4. Baryon to Total Mass Profiles

In this section, we analyze the stellar, hot gas, and baryon to total mass fraction profiles. The baryonic mass profile is defined as the sum of the stellar and hot gas components. The hot gas and total mass profiles are measured using the method described in Bo17 and that we will briefly summarize here. Deep (297 ks) *Chandra* X-ray observations (Ogrean et al. 2015) are used to measure the hot gas mass by fitting, in 2D, the X-ray surface brightness map with dual Pseudo-Isothermal Elliptical (dPIE) mass distributions. The best model for the hot gas consists of three spherical dPIE components. In turn, this is used as a fixed mass component in a standard strong lensing analysis of the cluster, from which the total, diffuse, and galaxy halo masses are measured. This method allows for a more self-consistent separation of the dark matter and hot gas components than a traditional approach. The CLASH and HFF images are complemented with MUSE data, allowing us to boost the number of spectroscopically confirmed multiple images to 102, making this one of the best data sets available for strong lensing analysis of a galaxy cluster. These data are used to infer the parameters of the cluster mass model, which consists of three large-scale halos (diffuse DM), the aforementioned hot gas component and 193 cluster member halos that include both the galaxy DM and stellar mass.

In Figure 2, we show the two-dimensional stellar, hot gas, and baryonic mass maps. In the left panels of Figure 2, we plot the total, stellar, hot gas, and baryonic surface mass density isocontours overlaid on a color-composite image of the cluster in seven *HST* optical filters. Right panels show the two-dimensional maps of the stellar, hot gas, and baryon to total mass fractions. We can see from Figure 2 that the stellar mass is concentrated mainly in the center, which is coincident with the position of the northern BCG, of the cluster and is embedded in the cluster members, while the hot gas contribution increases moving toward more external regions.

Using the same method as in Bo17, we derive the cumulative projected radial profile of the stellar mass component. In the first panel of Figure 3, we show the cumulative projected mass profile of the different components: total, diffuse halos (mostly DM), galaxy halos, stellar, and hot gas. This plot complements Figure 4 in Bo17 with the addition of the stellar component.

The statistical errors on stellar mass profile are derived by considering the minimum and maximum stellar $M_\star/L$ values defined in Section 3.2. In the second panel of Figure 3, we show the cumulative projected stellar and hot gas to total mass profiles of the cluster, obtained from the combination of this work and the strong lensing modeling (Bo17). In this plot, the statistical errors of the stellar mass component are significantly smaller than those of the total mass profile. We remark that the stellar mass values derived from an SED fitting depend on the adopted stellar templates and IMF.

The relative contribution of the cluster member subhalos to the total mass profile decreases moving from the cluster center, reaching approximately the same value of the hot gas component at a projected distance between 100 and 200 kpc. The diffuse DM mass component is the dominant one at all radii. The cumulative projected stellar over total mass fraction profile has a decreasing trend, with a peak value of $f_\star \sim 15\%$ near the cluster center and a mean value of 2% at 100 kpc from the center. The overall trend is in agreement with that found by Grillo et al. (2015).

The choice of the stellar IMF can change up to approximately a factor of 2 the estimated stellar mass to light ratio. Hoag et al. (2016) found for the same cluster a mean value of $f_\star$ of $\approx$0.9% within a square region of side $\sim$730 kpc and using a diet-Salpeter IMF. Bahcall & Kulier (2014) found a value of $f_\star$ of $\sim$1% for massive clusters (as massive as M0416) at redshift $z = 0.3$ using a Chabrier IMF (Chabrier 2003) at different radial ranges. If we consider the conversion factor between the different stellar IMFs, our values are consistent with those obtained in these previous works. We can also evaluate the cumulative projected stellar to total mass fraction in cluster members. This fraction reaches a maximum value of $\approx$35% near the cluster center and drops to a mean value of 15% at larger clustercentric distances. This fraction is in agreement with that estimated in the cores of SDSS massive early-type galaxies (e.g., Grillo 2010).

The cumulative projected baryonic to total mass fraction, considered as the summed contribution of galaxy stars and hot intracluster gas, starts from 15% in the cluster core, then has a minimum and finally increases up to approximately 10% at a projected distance of 350 kpc from the cluster center. These trends are in agreement with those found in Biviano & Salucci (2006), who analyzed the mean profiles of different mass components by using data from 59 nearby clusters from the ESO Nearby Abell Cluster Survey. The value of the baryonic mass fraction at large radii is also comparable with that obtained by Gonzalez et al. (2013) in clusters of similar mass. This fraction is smaller than the cosmological baryon fraction estimated from CMB measurements from Planck (0.147 ± 0.006, Planck Collaboration et al. 2016). However, this is not very surprising since this analysis is limited to the inner 300 kpc of M0416.

5. Dark Matter Profile

In this section, we analyze the surface mass density profiles of the different mass components. We remark that with our analysis we can disentangle the dark-matter-only component, as opposed to most of the previous studies.

In the left panels of Figure 4, we show the total matter, diffuse, and global dark-matter surface mass density profiles of M0416 fitted with NFW, Hernquist (1990) softened isothermal sphere (NIS; Grogin & Narayan 1996) and power-law profiles. The global dark-matter component is the sum of the diffuse term and that embedded in galaxy halos. The latter has been obtained from the total mass density profiles of the galaxies reconstructed in the lensing optimization and subtracting their stellar mass density profiles described above. From this plot, we can see that the total and global dark-matter surface mass density profiles are overall well fitted by NFW, Hernquist, and in the inner 100 kpc, power-law profiles, while an NIS profile provides a poor fit. For this reason, an NIS profile is not considered in the following.

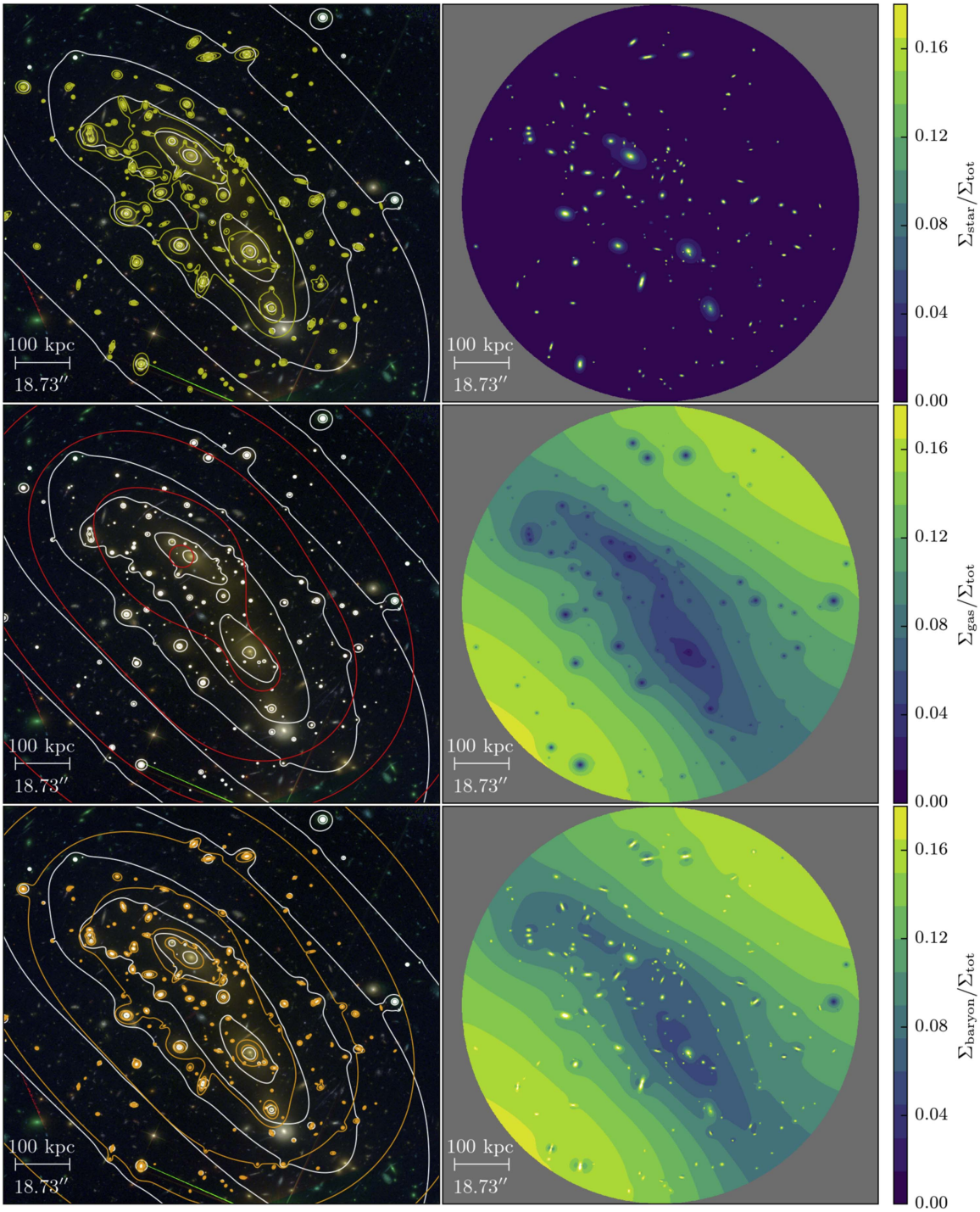

Figure 2. Left panels: total, stellar, hot gas, and baryonic surface mass density isocontours overlaid on a color-composite image of the cluster in seven optical filters. White lines are the total mass isodensity levels, which have a logarithmic step between 0.00035 and 0.003 $M_{\odot}$ kpc^{-2}. Yellow lines refer to the stellar mass isodensities and are spaced between 3.5×10^{-6} and $3 \times 10^{-4}\,M_{\odot}$ kpc^{-2}. Red lines are the hot gas isodensity contours spaced between 4.5×10^{-5} and $1.8 \times 10^{-4}\,M_{\odot}$ kpc^{-2}. Orange lines refer to the baryonic component (stars + hot gas) and have the same range as the hot gas component. Right panels show the two-dimensional surface density profile ratios of stellar (upper panel), hot gas (middle panel), and baryon (bottom panel) over total mass.

We compare the values of the parameters of the best-fitting NFW profile we derive for the total mass with those obtained from the weak lensing analysis by Umetsu et al. (2014). Our estimate of $M_{200,c}$ is $1.6 \times 10^{15}\,M_{\odot}$. Umetsu et al. (2014) measured $(1.04 \pm 0.22) \times 10^{15}\,M_{\odot}$ for the same cluster but with a slightly different cosmology. The discrepancy between these values might suggest that the fits of the separate strong and weak lensing data cannot be used to extrapolate correctly in the outer and inner regions, respectively, the total mass of M0416. However, we remark that the independent strong and weak lensing total mass estimates of M0416 nicely match in the overlapping region (see Figure 16 in Grillo et al. 2015) and are overall consistent with the results from the X-ray and dynamical analyses (see Figure 13 in Balestra et al. 2016).

From the left panels of Figure 4, we infer that due to projection effects, for models with two different inner and outer

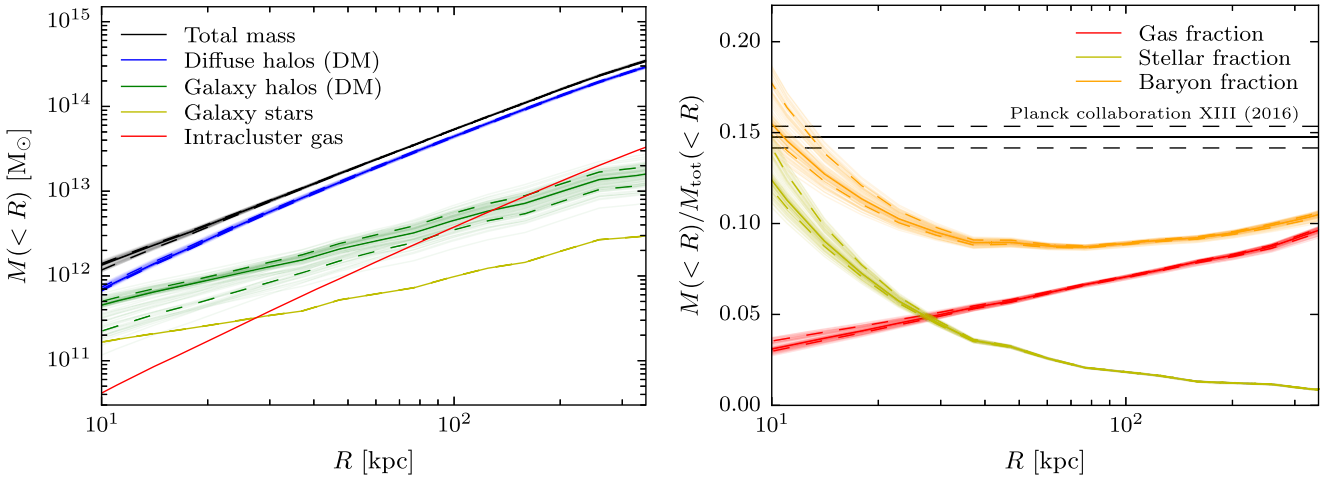

Figure 3. Left panel: cumulative projected mass profiles of the different cluster mass components. Right panel: ratio between the cumulative projected mass profiles of the baryonic components and the cumulative projected total mass profile. The solid and dashed black lines represent the value of the cosmological baryon fraction from Planck Collaboration et al. (2016) with the 1σ uncertainty.

slopes, the sum of multiple components (M0416 does not have a unimodal total mass distribution), and the "circularization" ($M(<R)$ and $\Sigma(R)$) of the profiles, contribute to the result of obtaining more than one model that is consistent with the reconstructed surface mass density profiles. In the very central region ($R \lesssim 15$ kpc), both the total matter and the global dark-matter profiles are steeper than cored profiles and NFW profiles. On the contrary, the DM diffuse profile is flatter. This can be explained considering that the center of the cluster is coincident with the position of the northern BCG, hence the steep total and global dark-matter profiles can be related to the dark-matter halo of the BCG.

In the right panels of Figure 4, we show the radial dependence of the logarithmic slope $\beta(R)$, defined as

$$\beta(R) = -\frac{d\ln\Sigma(R)}{d\ln(R)}. \quad (1)$$

In the case of a power-law profile $\gamma_{\rm in} = \beta + 1$ (see Section 1). In the other cases, the relation between the two slopes is more complex. This quantity has been calculated numerically for the total matter and global dark-matter surface profiles, as derived from the data and as predicted from the NFW, Hernquist, NIS, and power-law best fits. We evaluate the slope values only in the radial range between 5 and 100 kpc. In the very center of the cluster (i.e., the region dominated by the northern BCG), the total matter and global dark-matter density profiles are steeper than NFW and Hernquist models. The global DM profile is somewhat flatter than the total mass profile. The diffuse DM profile is significantly flatter than the others. In the diffuse DM component, the BCG is not included. The best-fit values of the logarithmic slope of the power-law fits, within the inner 100 kpc, are $\beta_{\rm tot} = 0.38 \pm 0.01$ and $\beta_{\rm DM} = 0.36 \pm 0.01$ for the total matter and global dark-matter profiles, respectively. We do not fit with this model the diffuse DM component because the slope cannot be well approximated by a single value.

Comparing our results to previous works is difficult because so far most observational studies have only focused on the total mass density profile (see Section 1). Newman et al. (2013a, 2013b) use a small sample of massive ($M_{200} = 0.4$–$2 \times 10^{15}\,M_\odot$), relaxed galaxy clusters, at $z = 0.19$–0.31, to measure the DM inner ($\lesssim$30 kpc) slope and compare it with that of the total mass and that predicted by simulations for collisionless dark-matter halos. They found that the slope of the observed total mass density profile ($\langle\gamma_{\rm in}\rangle = 1.16 \pm 0.05$) is in agreement with that predicted from DM-only simulations. They proposed a scenario according to which an early dissipative phase of star formation in the BCG establishes a steeper total mass density profile ($\rho_{\rm tot}$) in the inner regions of a cluster (5–10 kpc). The subsequent accretion of stars then mostly replaces the dark matter, so that the total mass profile is nearly maintained. In the same works, the observed DM profile was found to be significantly shallower ($\langle\gamma_{\rm in}\rangle = 0.5 \pm 0.1$) than canonical NFW models in the radial range $r \lesssim 30$ kpc, comparable with the effective radius of the BCG. In Newman et al. (2013a), it is argued that variations in the observed inner dark-matter profiles can be seen from cluster to cluster, correlating with the size and mass of the BCG. This would suggest a connection between the dark-matter profile in the cluster cores and the assembly of stars in the BCGs. Laporte & White (2015), using state of the art N-body resimulations of the growth of rich galaxy clusters between $z = 2$ and $z = 0$, show that the steeper and shallower profiles of, respectively, total mass and global dark matter found by Newman et al. (2013a) can be explained as the result of dissipationless mergers. Note that Newman et al. (2013a) and Laporte & White (2015) adopt definitions of the dark-matter profiles slightly different from ours. In Newman et al. (2013a), the dark-matter mass density profile was obtained by subtracting from the total mass density profile that of the BCG stellar component. Furthermore, Newman et al. (2013a) did not consider the intracluster hot gas, claiming that its inclusion would not change the shape of the dark-matter density profile. The definition of dark matter is close to our definition of global dark matter. The dark-matter component of Laporte & White (2015) is comparable to our definition of global dark-matter component (by construction). With this in mind, we do find an indication that the global dark matter is flatter than the total component, even if this difference is not significant. On the other hand, from Figure 5 of Newman et al. (2013a) a cluster with a BCG as small as the one in M0416 (in terms of effective

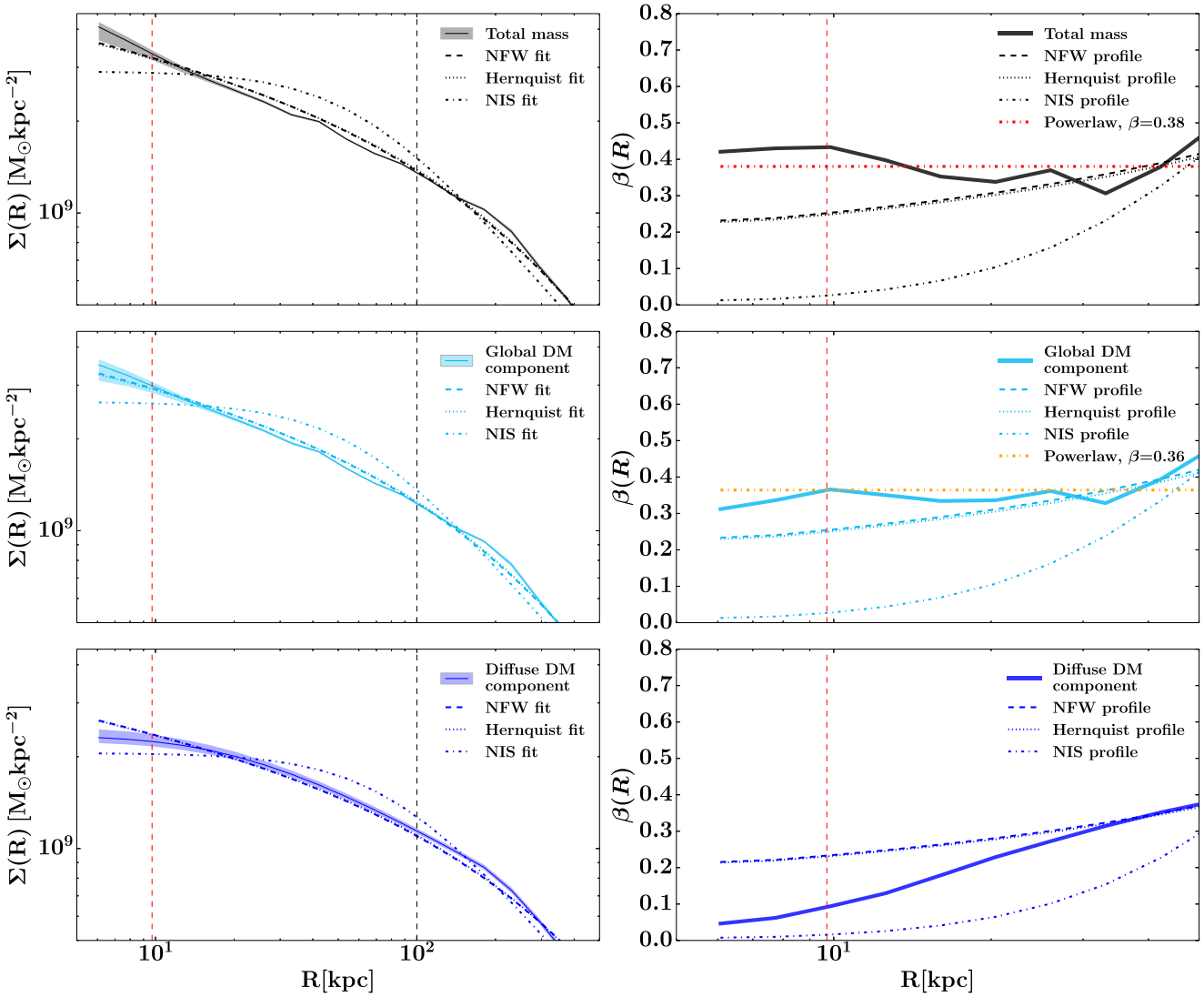

Figure 4. Left panels: surface mass density profiles of total (top row) and dark-matter (middle and bottom rows) components fitted with an NFW (Navarro et al. 1996), Hernquist (Hernquist 1990), and a softened isothermal sphere (NIS; Grogin & Narayan 1996) profile. Right panels: $\beta(R)$ defined as in Equation (1) calculated for the total (top row) and dark matter (middle and bottom rows) surface mass densities and compared with the values of NFW (dashed), Hernquist (dotted), softened isothermal sphere (dotted–dashed), fits. The red dashed lines show the effective radius of the BCG. The black dashed lines represent the radius where we see a change in the slope of the total surface mass density profile and represents also the range in which we have performed a fit with a power-law profile. To better show the differences, in the right panels, we focus on the inner 50 kpc.

radius) is expected to have a steeper dark-matter profile, hence much more similar to the total one.

6. Conclusions

In this work, we have decomposed the total mass profile of the galaxy cluster MACS J0416−2403 into its different components: stellar, hot gas, dark-matter diffuse and dark-matter substructures. To this aim, we have used state of the art lens models based on HFF imaging data and extensive VLT spectroscopy, as well as deep *Chandra* observations. We have determined the cumulative projected radial mass profiles and the surface mass density maps of these components. For the first time, we have been able to separate all components with little previous assumptions and also to map precisely the dark-matter-only distribution within 300 kpc from the cluster center.

Our main results can be summarized as follows.

1. The stellar and hot gas components are only a small percentage of the total matter in the cluster. The stellar mass contribution reaches the peak value of $f_* = 15\%$ within 20 kpc from the cluster center, due to the presence of the BCG, then decreases to a mean value of 2% at 100 kpc from the cluster center. The hot gas to total mass fraction, instead, increases with the distance from the center. The baryon fraction, evaluated as the sum of the stellar and hot gas components over the total mass of the cluster, has a peak value of 15% in the cluster center, then decreases reaching ∼10% at 350 kpc. Both the stellar and baryon fractions are in general good agreement with the global values found in the literature. Our baryon fraction is smaller than the cosmological baryon fraction measured by Planck Collaboration et al. (2016), which refers to large radii.
2. We have evaluated the ratio between the stellar and total mass embedded in substructures. This fraction is ∼30% near the cluster center, then decreases to ∼15% at larger clustercentric distances.
3. We have studied the total mass, global, and diffuse dark-matter surface density profiles. In the radial range between

5 and 50 kpc, the surface mass density profiles of the total mass and global dark-matter have comparable slopes. In this radial range, if we parametrize $\Sigma(R)$ as $R^{-\beta}$, we obtain values of β equal to 0.38 ± 0.01 and 0.36 ± 0.01 for the total and global dark matter, respectively. These profiles appear steeper than an NFW profile. The diffuse dark-matter component has a profile much flatter near the cluster center that cannot be approximated with a power law. The difference among these three profiles is related to the BCG dark-matter halo and persists up to $\sim$30 kpc from the cluster center, which is approximately three times the value of the effective radius of the BCG.

4. As a result of the mass decomposition presented in this work, we are able to confirm previous findings from Caminha et al. (2017) and Bo17 regarding the absence of a significant ($>3\sigma$) offset between the dark-matter and the stellar (BCGs) components. A secure detection of such offsets in merging systems would be important, since they are predicted by models of self-interacting dark matter (e.g., Markevitch 2006). We remark, however, that despite the accurate modeling of DM and baryonic components developed here, it remains very difficult to establish the presence of offsets of a few arcsec, due to a number of inherent systematics in the lens model, as well as line-of-sight lensing effects (Chirivì et al. 2017).

In the future, we plan to extend this analysis to other clusters from the CLASH sample with highly precise strong lensing data and MUSE spectroscopy.

We acknowledge support from PRIN-INAF 2014 1.05.01.94.02 (PI M. Nonino). M.B. and C.G. acknowledge support by the VILLUM FONDEN Young Investigator Programme through grant no. 10123. A.M. acknowledges funding from the INAF PRIN-SKA 2017 program 1.05.01.88.04.

ORCID iDs

M. Bonamigo https://orcid.org/0000-0002-1461-1115
C. Grillo https://orcid.org/0000-0002-5926-7143
A. Mercurio https://orcid.org/0000-0001-9261-7849
A. Biviano https://orcid.org/0000-0002-0857-0732
M. Girardi https://orcid.org/0000-0003-1861-1865
R. Gobat https://orcid.org/0000-0003-0121-6113

References

Agnello, A., & Evans, N. W. 2012, ApJL, 754, L39
Amorisco, N. C., & Evans, N. W. 2012, ApJL, 756, L2
Annunziatella, M., Biviano, A., Mercurio, A., et al. 2014, A&A, 571, A80
Annunziatella, M., Mercurio, A., Biviano, A., et al. 2016, A&A, 585, A160
Bahcall, N. A., & Kulier, A. 2014, MNRAS, 439, 2505
Balestra, I., Mercurio, A., Sartoris, B., et al. 2016, ApJS, 224, 33
Barden, M., Häußler, B., Peng, C. Y., McIntosh, D. H., & Guo, Y. 2012, MNRAS, 422, 449
Bertin, E., & Arnouts, S. 1996, A&AS, 117, 393
Biviano, A., & Salucci, P. 2006, A&A, 452, 75
Bonamigo, M., Grillo, C., Ettori, S., et al. 2017, ApJ, 842, 132
Bruzual, G., & Charlot, S. 2003, MNRAS, 344, 1000
Calzetti, D., Armus, L., Bohlin, R. C., et al. 2000, ApJ, 533, 682
Caminha, G. B., Grillo, C., Rosati, P., et al. 2017, A&A, 600, A90
Chabrier, G. 2003, PASP, 115, 763
Chirivì, G., Suyu, S. H., Grillo, C., et al. 2017, arXiv:1706.07815
Ebeling, H., Edge, A. C., & Henry, J. P. 2001, ApJ, 553, 668
Gonzalez, A. H., Sivanandam, S., Zabludoff, A. I., & Zaritsky, D. 2013, ApJ, 778, 14
Grillo, C. 2010, ApJ, 722, 779
Grillo, C. 2012, ApJL, 747, L15
Grillo, C., Suyu, S. H., Rosati, P., et al. 2015, ApJ, 800, 38
Grogin, N. A., & Narayan, R. 1996, ApJ, 464, 92
Hernquist, L. 1990, ApJ, 356, 359
Hoag, A., Huang, K.-H., Treu, T., et al. 2016, ApJ, 831, 182
Jauzac, M., Clement, B., Limousin, M., et al. 2014, MNRAS, 443, 1549
Laporte, C. F. P., & White, S. D. M. 2015, MNRAS, 451, 1177
Lotz, J. M., et al. 2016, arXiv:1605.06567
Markevitch, M. 2006, in ESA Special Publication 604, The X-ray Universe 2005, ed. A. Wilson (Paris: ESA), 723
Navarro, J. F., Frenk, C. S., & White, S. D. M. 1996, ApJ, 462, 563
Newman, A. B., Treu, T., Ellis, R. S., et al. 2013a, ApJ, 765, 24
Newman, A. B., Treu, T., Ellis, R. S., & Sand, D. J. 2013b, ApJ, 765, 25
Ogrean, G. A., van Weeren, R. J., Jones, C., et al. 2015, ApJ, 812, 153
Okabe, N., & Smith, G. P. 2016, MNRAS, 461, 3794
Peng, C. Y., Ho, L. C., Impey, C. D., & Rix, H.-W. 2010, AJ, 139, 2097
Planck Collaboration, Ade, P. A. R., Aghanim, N., et al. 2016, A&A, 594, A13
Postman, M., Coe, D., Benítez, N., et al. 2012, ApJS, 199, 25
Rocha, M., Peter, A. H. G., Bullock, J. S., et al. 2013, MNRAS, 430, 81
Rosati, P., Balestra, I., Grillo, C., et al. 2014, Msngr, 158, 48
Salpeter, E. E. 1955, ApJ, 121, 161
Springel, V., Frenk, C. S., & White, S. D. M. 2006, Natur, 440, 1137
Umetsu, K., Medezinski, E., Nonino, M., et al. 2014, ApJ, 795, 163
Umetsu, K., Zitrin, A., Gruen, D., et al. 2016, ApJ, 821, 116